Rapid Communications   Editors' Suggestion

Property and cation valence engineering in entropy-stabilized oxide thin films

George N. Kotsonis [1,*] Peter B. Meisenheimer [2] Leixin Miao,[1] Joseph Roth,[1] Baomin Wang,[3] Padraic Shafer,[4] Roman Engel-Herbert,[1] Nasim Alem,[1] John T. Heron,[2] Christina M. Rost,[5] and Jon-Paul Maria[1]

[1]*Department of Materials Science and Engineering, The Pennsylvania State University, University Park, Pennsylvania 16802, USA*
[2]*Department of Materials Science and Engineering, University of Michigan, Ann Arbor, Michigan 48108, USA*
[3]*Department of Electrical Engineering, The Pennsylvania State University, University Park, Pennsylvania 16802, USA*
[4]*Advanced Light Source, Lawrence Berkeley National Laboratory, Berkeley, California 94720, USA*
[5]*Department of Physics and Astronomy, James Madison University, Harrisonburg, Virginia 22807, USA*

We present data for epitaxial thin films of the prototypical entropy-stabilized oxide (ESO), $Mg_{0.2}Ni_{0.2}Co_{0.2}Cu_{0.2}Zn_{0.2}O$, that reveals a systematic trend in lattice parameter and properties as a function of substrate temperature during film growth with negligible changes in microstructure. A larger net Co valence in films grown at substrate temperatures below 350 °C results in a smaller lattice parameter, a smaller optical band gap, and stronger magnetic exchange bias. Observation of this phenomena suggests a complex interplay between thermodynamics and kinetics during ESO synthesis; specifically thermal history, oxygen chemical potential, and entropy. In addition to the compositional degrees of freedom available to ESO systems, subtle nuances in atomic structure at constant metallic element proportions can strongly influence properties, simultaneously complicating physical characterization and providing opportunities for property tuning and development.

I. INTRODUCTION

Rost *et al.*'s report on entropy-stabilized oxide (ESO) in 2015 demonstrated a paradigm in which crystalline oxide solutions are enabled by configurational entropy. The prototypical ESO, $Mg_{0.2}Ni_{0.2}Co_{0.2}Cu_{0.2}Zn_{0.2}O$, hereafter designated J14, equilibrates in a rocksalt-structured solid solution above ≈875 °C in ambient atmosphere. Single-phase solution formation involves a negative change in Gibbs free energy, $\Delta G = \Delta H - T\Delta S$, occurring via an increase in entropy ΔS, at the expense of a positive change in enthalpy $\Delta H \approx$ 12 kJ/mol [1]. A large configurational entropy and positive enthalpy are distinguishing ESO features. The J14 simple rocksalt crystal structure and low transition temperature from a phase-segregated mixture to solid solution makes it a natural prototype for investigating trends in ESO systems.

Homogeneous J14 solutions and related ESOs possess characteristics giving rise to atypical physics and materials design opportunities: cations occupying uncommon bonding environments and local symmetry breaking in a crystal with otherwise high-fidelity long-range order [2]. For example, Jahn-Teller distortions of CuO_6 octahedra in single-phase J14 give rise to local tetragonality in a macroscopically cubic crystal [2–4]. ESO systems also possess noteworthy compositional flexibility. J14-derived rocksalt solutions can host Cu or Co concentrations upwards of 27% [4–6] and are amenable to aliovalent incorporations of Li or Na; or co-incorporation of Li-Ga or Li-Fe pairs [7–9]. Studies on charge compensation for aliovalent additions indicate complex contributions from both oxygen vacancies and cation charge transfer [10–12], illustrating a tolerance for multivalency and vacancies in ESOs.

Physically, ESO crystals exhibit intriguing properties and tunability. Lattice distortions and charge disorder in ESO systems result in suppressed thermal transport [13–15], while compositional flexibility results in electrochemical utility [7,16–18]. Optical tunability has been observed via cation selection [8,19] and cation valence control [20]. Combined charge, spin, and orbital degrees of freedom manifest in diverse and tunable magnetic responses [21]. J14 exhibits long-range antiferromagnetic ordering, despite the presence of nonmagnetic Mg^{2+} and Zn^{2+} [9,22,23]. Composition-dependent spin frustration in related rocksalt ESOs permits tunable Néel temperatures [9] and enhanced magnetic exchange coupling when interfaced with a ferromagnet [5,6].

A common assumption in ESO research is compositional homogeneity. Thorough characterization suggests phase purity and compositional homogeneity in thermally quenched J14 specimens [1,24]. However, ESO solid solutions possess inherent metastability at low temperatures, where multiphase or chemically segregated states are globally stable [1,4,25–27]. Due to this metastability, it is prudent to explicitly consider processing conditions when studying ESO specimens; particularly thermal history, synthesis kinetics, and partial oxygen pressure (pO_2).

Tendencies for metastable behavior are strong in ESOs prepared using pulsed-laser deposition (PLD). Prior reports show that highly misfit cations such as Sc, Cr, Ge, Sn, or Sb, can be metastably dissolved into J14 at equimolar concentrations via PLD, while bulk attempts result in multiphase material [28]. Kotsonis *et al.* attributed this to a mechanism where the effective temperature of laser plasma species produces an effective
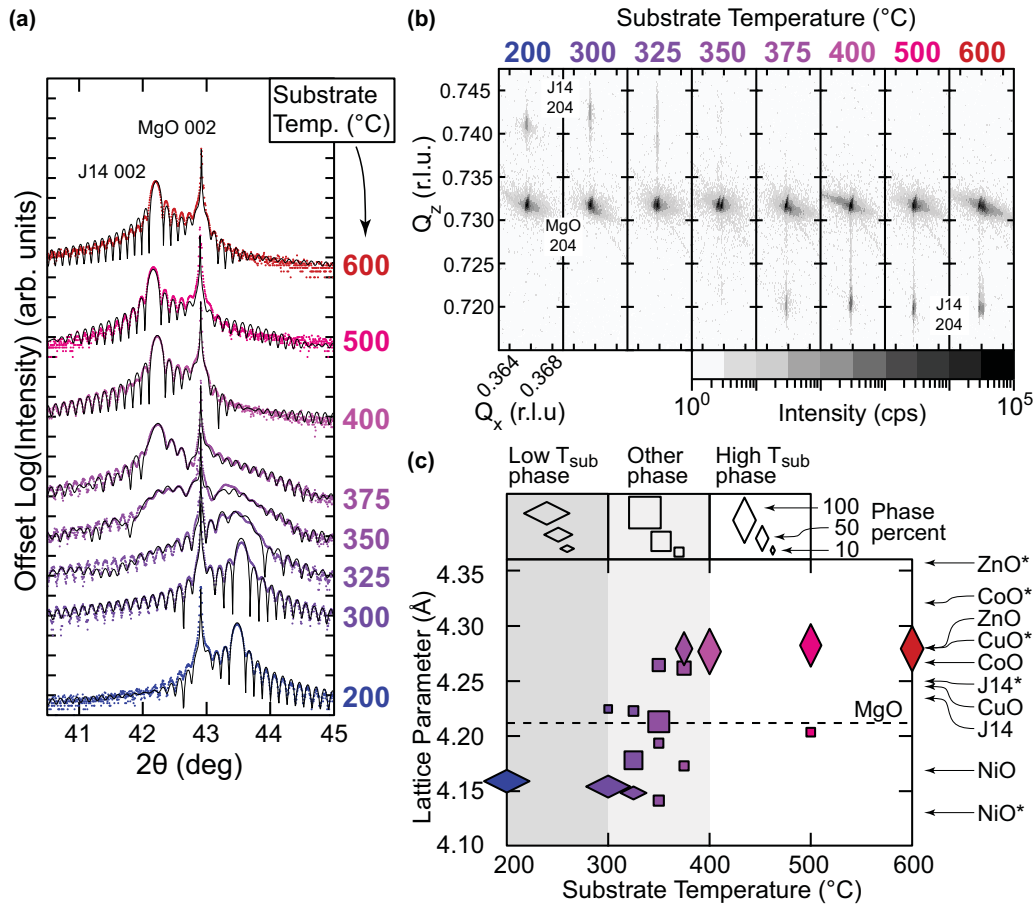
*Corresponding author: gnk5@psu.edu

FIG. 1. Structural data for J14 films: (a) offset symmetric θ-2θ diffraction patterns (colorful dots) and corresponding fits (black lines); (b) reciprocal space maps of film and substrate 204 reflections; and (c) plot of fitted lattice parameters including relaxed and epitaxially strained (*) reference materials [2,30,32–40]. In (c), marker shape and size correspond to fitted phase and phase percent, respectively, indicated by the legend.

TS term (in $G = H - TS$) upon condensation, thus promoting assembly of the high-entropy solid solution state [29]. The rapid quench after landing freezes the high temperature structure, which persists indefinitely (by current observations) at ambient temperature. If such mechanisms occur in other ESO systems, there are possibilities to explore structures far from equilibrium and potentially modulate growth conditions to tune properties.

As an initial investigation of such effects, we present property trends in epitaxial J14 thin films as a function of substrate temperature in the range between 200 °C and 600 °C with all other deposition parameters constant. Complementary data from diffraction, microscopy, spectroscopy, ellipsometry, and magnetometry suggests that substrate temperatures below 350 °C favor a higher net valence state for Co cations, concomitant with a reduced unit cell volume, a smaller optical band gap, and an enhanced magnetic exchange bias. These features collectively represent a kinetically accessible, isostructural "phase" with different physical properties than films grown above 350 °C. At higher deposition temperatures, recovered films appear similar to the high-temperature phase of bulk J14. These observations suggest that compositionally complex systems may contain many such nonequilibrium phases, distinguishable by combinations of lattice distor-

tions and cation valence, exhibiting interesting property opportunities.

II. RESULTS AND DISCUSSION

Preliminary studies on epitaxial J14 films by Rost revealed an unusually sharp discontinuity in the out-of-plane lattice parameter as a function of substrate temperature with no apparent change in crystal quality [28]. Robust reproducibility of this phenomena prompted follow-up studies, discussed here, to uncover the origin of the trend and corresponding changes in film properties. Films were grown by PLD on [001]-MgO substrates in 50 mTorr flowing O_2 from a single-phase J14 target (Fig. S1 [30]). Substrate temperature varied from 200 °C to 600 °C. Figure 1(a) presents θ-2θ x-ray diffraction (XRD) patterns and corresponding data fits [31], which considered multiple rocksalt phases (geometrically arranged as layers) to account for a potential distribution of lattice parameters. All films are epitaxially strained rocksalt phases commensurate to the substrate (i.e., in-plane lattice parameters $a = b = 4.21$ Å), evidenced from reciprocal space maps in Fig. 1(b). Out-of-plane lattice parameters, phases, and phase fractions extracted from XRD models are compiled in Fig. 1(c) with predicted values for relaxed and fully strained J14 and
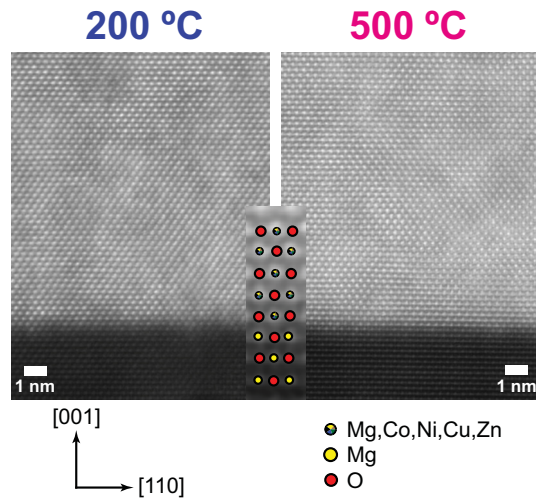
FIG. 2. HAADF-STEM images viewed along the $[\bar{1}10]$ zone axis of J14 films grown at 200 (left) and 500 °C (right). Center inset is magnified from the 500 °C film/substrate interface to show atomic positions.

constituent oxides in rocksalt structures for reference [2,30,32–40].

The out-of-plane lattice parameter shifts from 4.28 Å for high temperature deposition to 4.16 Å for low temperature deposition. In terms of unit cell volume, substrate temperatures $\geqslant 400$ °C promote a phase similar to bulk J14 [2], while substrate temperatures $\leqslant 300$ °C result in a phase with smaller unit cell volume. Acceptable XRD fits for intermediate substrate temperatures (300–400 °C) required models with multiple coexisting phases. Small deviations between data and fits in this regime are attributed to multi-interference Kiessig fringe effects originating from the abrupt interfaces intrinsic to these models. Realistically, the films likely possess a smoother spatial distribution of lattice parameters. Diffraction analysis suggests two well-defined growth regimes and a transitional growth regime characterized by a lattice parameter distribution, likely due to complex interplay of free energy contributions from each phase, including strain energy and entropy.

Rocking curve peaks for all films exhibit full width at half maxima less than 0.025°, indicating low mosaicity (Fig. S2 [30]). High-angle annular dark-field scanning transmission electron microscopy (HAADF-STEM) for films grown at 200 °C and 500 °C is presented in Fig. 2; representative of the low- and high-substrate temperature phases, respectively. Image analysis confirms single-phase rocksalt structure and coherent film/substrate interfaces. Further, for films in both growth regimes, energy-dispersive spectroscopy indicates a uniform cation distribution (Figs. S3 and S4) and atomic force microscopy (AFM) image analysis indicates root-mean-squared surface roughness <1 nm (Fig. S5) [30].

Combined XRD, HAADF-STEM, and AFM results show strained rocksalt films with comparable crystalline perfection, but a phase transition where unit cell dimensions switch abruptly from $c > a = b$ to $c < a = b$ below a threshold substrate temperature. The magnitude of this lattice parameter shift is notably large. J14 experiences a 2.8% change in out-of-plane lattice parameter at constant laser fluence and $p\mathrm{O}_2$,

triggered by only a 50 °C change in growth temperature. For comparison, nonstoichiometric PLD-grown SrTiO₃ lattice parameters can deviate up to 2% from bulk depending on plume dynamics (i.e., laser fluence, $p\mathrm{O}_2$, total pressure, working distance, etc.) [41,42]. However, with constant plume dynamics, epitaxial SrTiO₃ out-of-plane lattice parameters vary by less than 1% as a function of substrate temperature [43].

To uncover the origins of this transition, we first turn to electron energy loss spectroscopy (EELS) measurements, which can selectively probe the core-level electronic structure for the multivalent transition metal elements Co, Ni, and Cu. For transition metals, the integrated intensity ratio from the L_3 and L_2 absorption edges is a useful parameter for determining valence state [44]. The Ni and Cu spectra for films grown at 200 °C and 500 °C are similar, but a difference in the Co spectra emerges (Fig. S6 [30]). Calculated Co L_3/L_2 ratios are 3.60 and 4.46, extrapolating to approximate net valences of 2.4 and 2.1, respectively. These values, along with reference values for Co-containing compounds are plotted in Fig. 3(a) [45].

To complement our EELS data, x-ray absorption spectroscopy (XAS) was performed on films grown at 200 °C and 600 °C. Similar to EELS, XAS of the Co L absorption edges is sensitive to Co valence. XAS is also sensitive to the Co spin state, due to selection rules in the photon-electron interaction. Co XAS spectra were fit to a linear combination Co³⁺ (Co₂O₃) and Co²⁺ (CoO) reference spectra [6,46] to determine relative valence state. Measured data, fits, and fit components are shown in Fig. 3(b). Fits approximate 30% high spin Co³⁺ in the 200 °C film (a net valence of 2.3) and nearly 100% Co²⁺ in the 600 °C film, in general agreement with EELS results. Ultimately, XAS and EELS both suggest a larger population of Co³⁺ in films grown in the low-substrate temperature regime. From tabulated ionic radii, we know that high spin Co³⁺ is 18% smaller than high spin Co²⁺ [47]. Thus, local strains and net lattice contraction are expected for higher Co³⁺ concentrations. From EELS, XAS, and tabulated ionic radii, we can then associate the unit cell volume change with a valence transition as a function of substrate temperature; low-temperature film growth corresponding to a phase with smaller lattice parameters and significant Co³⁺ concentrations.

To understand the evolution of Co valence as a function of substrate temperature, we first consider the relative stability of CoO (all Co²⁺) and Co₃O₄ (2:1 Co³⁺:Co²⁺ ratio) as a function of temperature and $p\mathrm{O}_2$. In ambient $p\mathrm{O}_2$ (160 Torr), Co₃O₄ is the stable phase below ≈900 °C [48]. For CoO crystals stabilized by quenching after growth, a Co₃O₄ surface layer forms when exposed to low temperatures in ambient $p\mathrm{O}_2$ [49]. The $p\mathrm{O}_2$ required to stabilize CoO at 600 °C is on the order of 1–10 mTorr O₂, close to our deposition pressure, but decreases exponentially with decreasing temperature [48]. With this in mind, we now consider Co valence in J14 synthesized under different conditions. Bulk samples equilibrated and quenched from $\geqslant 900$ °C in ambient $p\mathrm{O}_2$ exhibit all Co²⁺ [8,18]. However, during low temperature film growth, a substantial fraction of Co prefers 3+ valence, consistent with the relative instability of CoO at low temperatures and high $p\mathrm{O}_2$. The growing film thus experiences a competition between the high chemical potential of oxygen, which favors Co³⁺, the lattice strain in J14, which favors Co²⁺, and configurational
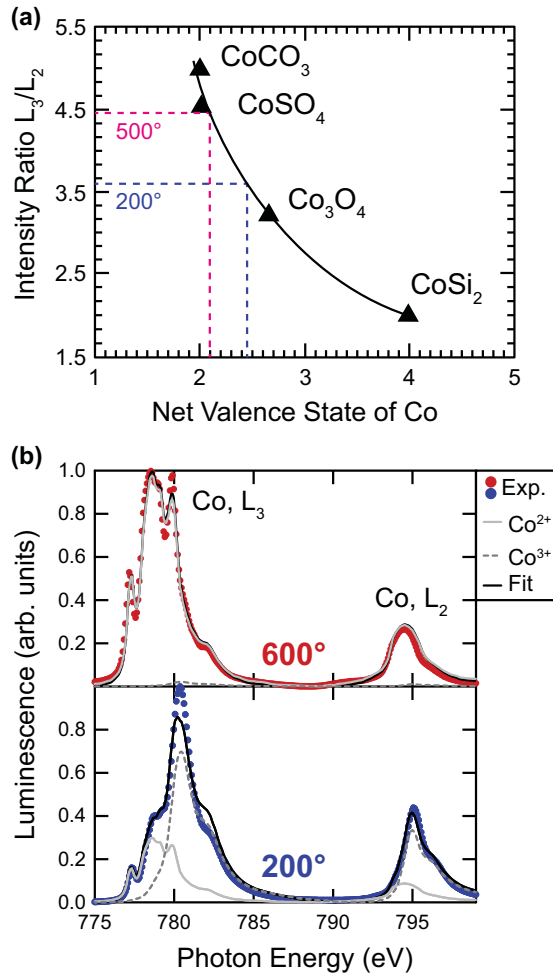
FIG. 3. Co valence state analysis: (a) integrated EELS L_3/L_2 intensity ratios and extrapolated net Co valence for films grown at 200 (dashed blue lines) and 500 °C (dashed red lines); and (b) normalized x-ray absorption spectra for films grown at 200 °C and 600 °C, fits indicate ≈30% Co^{3+} and ≈70% Co^{2+} for the 200 °C film and nearly 100% Co^{2+} for the 600 °C film. In (a), figure and reference data adapted from Ref. [45] with permission from the authors and publisher; Copyright (2000) Elsevier. In (b) Red/blue dots represent experimental data, solid gray lines represent the Co^{2+} reference component, dashed gray lines represent the Co^{3+} reference component, and black lines represent the final fit.

FIG. 4. Optical models for J14 thin films determined from ellipsometry: (a) real component of the refractive index n; (b) imaginary component of the refractive index k; (c) band edge parameter for the lowest energy (Tauc-Lorentz) oscillator in the model; and (d) real (circles) and imaginary (squares) components of the refractive index at 1240 nm. Temperature labels in (a) represent substrate temperature during film growth.

entropy, which favors the high-symmetry rocksalt structure. We speculate that the large and rapidly quenched kinetic energy of PLD adatoms amplifies the TS contribution to the free energy, driving the assembly of a rocksalt phase with enhanced Co^{3+} concentrations compared to bulk samples. We suspect charge neutrality for Co^{3+} is provided by oxygen uptake and cation deficiency rather than charge transfer; EELS and XAS do not suggest changes in Cu or Ni valence (Figs. S6 and S7 [30]). The entropy-stabilized nature of J14 appears to disperse the Co^{3+} enough to prevent the nucleation of Co_3O_4 or other higher oxide phases, which commonly occurs in binary transition metal rocksalt oxide films to accommodate cation oxidation to 3+ [50–52]. Judging from our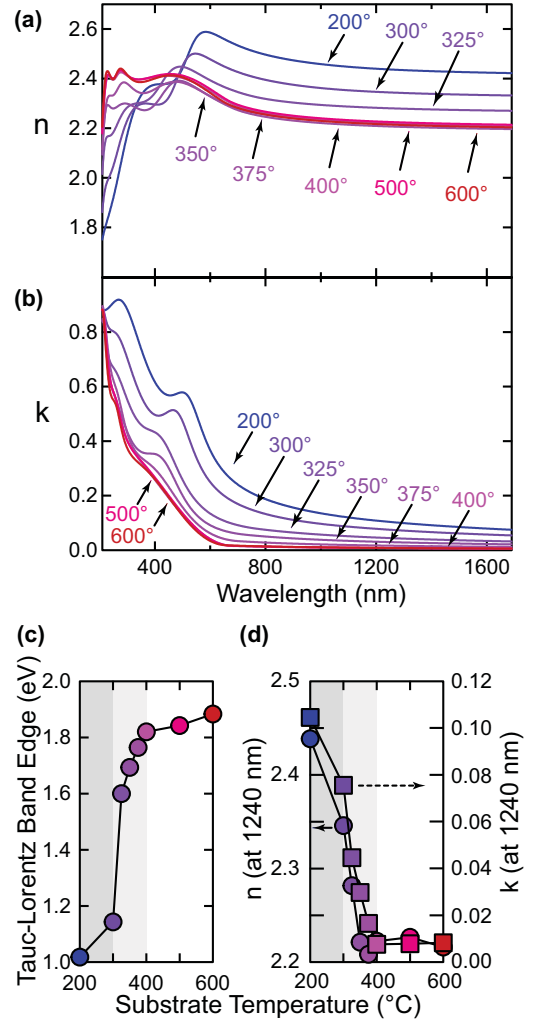 structural models, 400 °C likely represents a threshold temperature, below which Co^{3+} is incorporated into the rocksalt structure and above which metastable Co^{3+} converts to a more stable 2+ state at the growing surface to produce a phase similar to bulk J14.

To investigate the consequence of variable Co valence, we identify two material properties that are sensitive: the complex refractive index $\bar{n} = n + ik$ (related to complex dielectric permittivity $\bar{\epsilon}$, via $\bar{n}^2 = \bar{\epsilon}$) and low-temperature magnetic response. Visual inspection and transmittance measurements suggest a significant change in optical band gap depending on substrate temperature (Fig. S8 [30]). Ellipsometry was performed to further characterize optical trends concurrent to the lattice parameter shift. Fitted models consist of one Tauc-Lorentz (T-L) and two Lorentz oscillator functions [30]. The T-L function allows for a low-energy cutoff (the "band edge" parameter) and asymmetric line shape, necessary for a consistent model across the film series. Figures 4(a) and
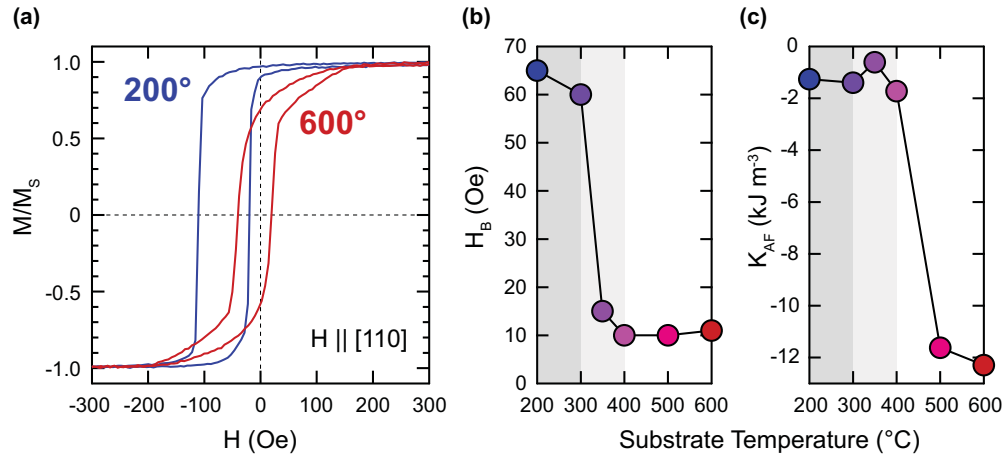
FIG. 5. Magnetometry data for J14 thin films grown across the investigated substrate temperature range: (a) example exchange biased magnetic hysteresis loops of the heterostructures with films grown at 200 °C (blue) and 600 °C (red) taken at 10 K along the [110] crystallographic direction after cooling to in a 2 T field, normalized to the saturation magnetization M_S; (b) exchange bias fields H_B; and (c) anisotropy constants K_{AF}.

4(b) present refractive index models from ellipsometry as a function of wavelength. Dispersions for 400–600 °C films are similar, but as substrate temperature decreases below 400 °C, features in k (related to absorption coefficient $\alpha = \frac{4\pi k}{\lambda}$, and wavelength λ), shift to longer wavelengths and increase in magnitude. Considering the optical response of native Co oxides in the context of their net Co valence, Co_3O_4 possesses a smaller band gap and additional low-energy optical transition compared to CoO [50]. Similarly, J14 films with enhanced Co^{3+} concentrations possess a smaller band gap and more pronounced absorption features.

The shift in band edge and appearance of the k maxima near 500 nm are linked to the band edge parameter of the T-L function; the lowest energy function in the model. The enhancement of the absorption tail (commonly called an Urbach tail [53]) can be parametrized by evaluating the refractive index below the T-L band edge. Figures 4(c) and 4(d) present the band edge parameter and refractive index at 1240 nm, illustrating the strong correlation between the optical trend, lattice parameter trend, and therefore net Co valence. We qualitatively attribute the Urbach tail to electronic disorder and local strain inherent to J14. Enhanced Co^{3+} concentrations appear to dramatically increase the degree of electronic disorder concurrent to enhanced lattice distortion from the small Co^{3+} radius, manifesting in a large optical absorption tail.

While ellipsometry probes excited electronic states, low-temperature magnetometry is sensitive to the magnetic phase near the ground state. Frustrated antiferromagnetic films can be characterized by measuring exchange bias, the exchange interaction across the interface with a soft ferromagnet [54,55]. Magnetic frustration in the antiferromagnetic layer is known to affect the magnitude of bias and coercive fields in the heterostructure, providing a pathway for studying antiferromagnetism in ESO systems. Accordingly, films were capped with thin layers of permalloy and Pt to create exchange bias heterostructures for magnetometry, as described previously [5,6].

Figure 5 presents magnetometry data collected at 10 K for the exchange bias heterostructures, showing changes in the bias field (H_B), coercive field, and magnetocrystalline anisotropy (K_{AF}). At high substrate temperatures, samples show a modest H_B with a large K_{AF}, a trend which inverts below the lattice parameter transition region around 350 °C. All magnetic hysteresis loops can be found in Fig. S9 [30].

The trend in H_B can be explained by looking to the spin glass model for exchange bias [56,57]. In the model, the parameter $R = \frac{K_{AF} \, t_{AF}}{f \, J_{AB}}$ defines the strength of the antiferromagnetic layer. Here t_{AF} is the layer thickness, f (a value between 0 and 1) is the degree of interface spin order, and J_{AB} is the interface exchange energy. Reported previously [6], these materials contain a large degree of magnetic frustration ($f \cong 0.3 \pm 0.1$), far from a more ideal antiferromagnet such as CoO ($f \cong 0.8$). In a regime where f is less than ≈ 0.9, H_B tends to decrease approximately monotonically with increasing R [56], thus large R can be seen to symmetrize the magnetic hysteresis and vice versa. Previously, varying Cu concentration was found to influence f via spin frustration from Jahn-Teller distortions [6]. However, here we assume a constant f since composition is not changing and look to K_{AF} and J_{AB} to identify the cause for the change in H_B and R.

K_{AF} is directly proportional to R, thus when K_{AF} becomes large, the loop should become more symmetric about the field axis and reduce H_B, in agreement with our present observations. R is inversely dependent on J_{AB}, which is a function of the number of uncompensated spins at the ferromagnet/antiferromagnet interface [56]. As J14 transitions from almost completely Co^{2+} (a magnetic d^7 cation) to a large fraction of magnetically inert $Co^{3+}(d^6)$, the system becomes more magnetically dilute, resulting in more uncompensated spins at the interface, larger J_{AB}, and a nonlinear decrease in R and increase in H_B. As both phenomena, magnetic dilution and change in anisotropy, occurred across the 300 °C–400 °C transitional temperature window, the magnetic transition

cannot be adequately described by only one of the parameters. This helps to explain why the steps in H_B and K_{AF} do not occur at precisely the same point. The observed magnetic transition can be directly linked to magnetic dilution from the change in Co oxidation state, commensurate with structural and optical trends. This shows that magnetic structure, in addition optoelectronic properties, can be finely tuned utilizing thin film deposition kinetics.

Further, we note that the phenomena under consideration are not unique to commensurate growth on MgO substrates. J14 grows on [00.1]-Al_2O_3 substrates with a [111] out-of-plane crystallographic orientation and exhibits a coinciding out-of-plane lattice parameter shift (Fig. S10 [30]). Additionally, pronounced lattice parameter dependences on growth conditions can also be observed in J14-derived six-component ESO systems containing Sc, Cr, Sn, Ge, or Sb [28], suggesting similar trends attributable to deviations from an ideal $A^{2+}O^{2-}$ rocksalt structure may exist for other ESO systems, facilitated by the interplay between thermodynamics, configurational entropy, multivalent cations, and nonequilibrium synthesis kinetics.

III. CONCLUSIONS

The collected data clearly illustrates a cooperative property shift as a function of substrate temperature for epitaxial J14 films. Substrate temperatures below $350\,^\circ$C result in films with enhanced Co^{3+} concentrations, 2.8% smaller unit cell volume, smaller direct optical band gap, and stronger magnetic exchange bias. Growth temperatures $\geqslant 400\,^\circ$C produce a state closer to that of bulk J14, with predominantly Co^{2+} cations. We tentatively attribute charge compensation for Co^{3+} in J14 primarily to cation vacancies, acknowledging that the general complexity and entropy-stabilized nature of ESOs can lead to sophisticated charge neutrality conditions and structural nuances. For example, preferential alignments of Jahn-Teller distorted CuO_6 octahedra may be influencing local strain energies or contributing to the relative sharpness of the lattice parameter change. More generally, the present observations suggest a complex interplay between entropy, kinetics, oxygen chemical potential, and strain energy during ESO crystal growth that can strongly affect charge distribution and properties. In addition to the compositional degrees of freedom available to ESO systems, subtle nuances in atomic structure at constant metallic element proportions can strongly influence the properties of ESO crystals, simultaneously complicating physical characterization and providing opportunities for property tuning and development.

APPENDIX A: SAMPLE SYNTHESIS

A single-phase J14 ceramic ablation target was sintered from a stoichiometric binary oxide powder mixture MgO ($\geqslant 99$%), CoO ($\geqslant 99$%), NiO (99.99%), CuO (99.99%), and ZnO (99.999%) in air at $1000\,^\circ$C for 12 h and air quenched. Target phase purity was confirmed by XRD (Fig. S1 [30]). J14 thin films were deposited on [001]-MgO substrates by PLD at substrate temperatures between $200\,^\circ$C and $600\,^\circ$C in flowing O_2 at a pressure of 50 mTorr to a nominal thickness of 75 nm. Laser repetition rate was 6 Hz and laser fluence was 1.2 J/cm^2. Substrates were cleaned with acetone, isopropanol, and methanol followed by a 10-min UV-ozone treatment.

APPENDIX B: STRUCTURAL CHARACTERIZATION

Surface morphology was measured using an Asylum MFP3D atomic force microscope in tapping mode. Crystal structure and lattice parameters of the as-deposited films were determined using a PANalytical Empyrean diffractometer. Optics included a 2-bounce Ge monochromator and 0.18° parallel plate collimator with proportional Xe detector. Reciprocal space maps employed a PIXcel^{3D} detector. Rocking curves were fit to a simple Gaussian function for full width at half maximum determination. Rocking curves are presented in Fig. S2 along with substrate rocking curves for comparison; MgO substrates are known to possess low-angle grain boundaries and multiple peaks in ω space [30,58]. Skew-symmetric θ-2θ scans and φ scans of 111 reflections confirm epitaxy and an in-plane epitaxial relationship of J14[100]$\|$MgO[100] (Fig. S11 [30]). Data for J14 grown on [00.1]-Al_2O_3 substrates is presented in Fig. S10, showing a coinciding lattice parameter trend. No x-ray reflections beyond that attributable to a rocksalt structure were observed in any films, particularly those of a spinel-type phase (e.g., Co_3O_4, $ZnCo_2O_4$, or similar solid solutions).

θ-2θ XRD patterns were fit using GenX software [31], considering multiple rocksalt layers to account for a potential distribution of lattice parameters. XRD fitting assumed a structure form factor averaged from nominal chemical composition with film thickness and lattice parameter as free fitting parameters. An additional unit-cell thick interface layer was included to account for a coherent offset between film and substrate [59] arising from potentially incomplete *in situ* removal of a surface contamination layer on the MgO substrates, which are prone to hydroxide formation. Commensurately strained lattice parameters for the constituent oxides and J14 in rocksalt structures were estimated using their respective Poisson ratios; the J14 Poisson ratio approximated as the average of constituents [2,32–40]. Fitting parameters, predicted lattice parameters, and Poisson ratios used are tabulated in Tables SI and SII [30].

APPENDIX C: ELECTRON MICROSCOPY, ENERGY DISPERSIVE SPECTROSCOPY, AND EELS

Transmission electron microscopy (TEM) samples of films grown at 200 °C and 500 °C were prepared using a Thermo Fisher Helios NanoLab Dual-Beam Focused Ion Beam (FIB) system. Samples were coated with carbon before and during FIB to protect the sample and improve conductivity during imaging. Cross-sectional FIB lamellas were lifted out onto a Molybdenum FIB TEM grid. FIB lamellas were first thinned down to around 500 nm using a 30-kV ion beam at 0.79 A, and then to around 50–100 nm using a 5-kV ion beam at 0.12 A. To reduce the redeposition and amorphization on the sample surface, a 2-kV and 1-kV ion beam was used for final sample cleaning.

HAADF-STEM images and EELS spectra were acquired using a Thermo Fisher Titan^3 S/TEM equipped with a spherical aberration corrector, a monochromator and a Gatan imaging filter. For STEM imaging, it was operated at a 300-kV accelerating voltage with a probe convergence angle of 30 mrad. Each set of high-resolution STEM image data contains a pair of STEM images with 0° and 90° scanning direction, and drift in the images was corrected using a nonlinear drift correction algorithm [60]. Energy dispersive spectroscopy (EDS) was performed to analyze the compositional homogeneity of the films (Figs. S3 and S4 [30]).

For EELS spectra acquisition, the TEM was operated at 80 kV to minimize the electron beam damage. Multiple line-scan STEM-EELS spectra were acquired on both samples; 8–16 spectra from different locations on each sample were added up to provide statistical significance. Each spectrum in the data set was measured with an exposure time of 10 s to obtain a large signal-to-noise ratio and sufficient counts. Normalized EELS spectra are plotted in Fig. S6 [30]. The locations of the core loss edges were calibrated with the location of the zero-loss peak from the low-loss spectra, acquired simultaneously. When calculating the L_3/L_2 intensity ratio, the background before the white lines was first fitted with a power law and subtracted. The background intensity within the white lines were modeled and subtracted by step functions, with the ratio of the step height to be 2:1, which corresponds to the ratio of electrons in the initial state of $2p$ orbitals [45].

APPENDIX D: X-RAY ABSORPTION SPECTROSCOPY

XAS spectra for films grown at 200 °C and 600 °C were measured at the Advanced Light Source at Lawrence Berkeley National Laboratory on beamline 4.0.2. XAS data was recorded at room temperature. Spectra for Co, Ni, and Cu L edges were collected. Spectra were normalized over eight scans per element, and data reported here shows the x-ray absorption that was calculated using luminescence yield collected from samples. This detection mode uses a photodiode to collect visible luminescence from the substrate (i.e., scintillator) to measure the intensity of x rays transmitted through the film. Spectra were measured with linearly polarized x rays; both horizontal and vertical polarizations were used. At every photon energy, absorption intensity was scaled to the flux of incoming x rays. Spectra were normalized so that their polarization-averaged intensity ranges from 0 to 1. Ni and Cu L edge spectra possess no discernable difference between films (Fig. S7 [30]). Co L edge spectra were fit to a linear combination of reference spectra for Co^{2+}, Co^{3+} (low spin), and Co^{3+} (high spin) from Ref. [46] using a basin-hopping optimization technique as implemented in Scipy for Python3. The low spin Co^{3+} fraction was eliminated as a result of the fitting and is therefore not shown.

APPENDIX E: SPECTROSCOPIC ELLIPSOMETRY

Spectroscopic ellipsometry was performed on a J.A. Woollam RC-2 ellipsometer. Scans were taken at incident angles of 50°, 60°, and 70°. Data was analyzed with the J.A. Woollam CompleteEASE software package. The MgO substrate was modeled with a Cauchy dispersion formula, determined separately from a bare substrate. Films were assumed to have uniform and isotropic optical constants. A superposition of three oscillators (one Tauc-Lorentz and two Lorentz [61]) was sufficient to describe optical constants for all films. The imaginary permittivity was modeled by the collection of oscillators with the real component coming from the Kramers-Kronig transform. Fitted film thicknesses agreed with x-ray reflectivity measurements to within a couple nm. Roughness for optical models was constrained to ⩽3 nm in accordance with the low roughness suggested by AFM. The figure of merit, the mean-squared-error (NCS weighting [62]), converged to <2.5 for all models presented. Figure S12 presents the permittivity as a function of energy for films grown at 300 °C and 400 °C, showing the evolution of the three oscillator components [30]. Corresponding raw ellipsometry data (Ψ and Δ as a function of wavelength) along with that of the fitted models is presented in Fig. S13. Table SIII presents all fitted parameters with uncertainties (90% confidence interval). Oscillator parameters are plotted against substrate temperature in Fig. S14 [30].

APPENDIX F: MAGNETOMETRY

Exchange bias heterostructures consisted of ∼5 nm of permalloy deposited directly on the ESO film by PLD, then capped with ∼10 nm of Pt to prevent its oxidation [5,6]. Heterostructures were measured along the [100] and [110] crystallographic directions in a QuantumDesign Dynacool physical property measurement system at 10 K after cooling from room temperature in a 2-T training field. Hysteresis loops were fitted using methods described previously [5,6]. Magnetic anisotropy was calculated from the relation $4K_1 = (A_{110} - A_{100})$, where A_{hkl} is the energy lost from magnetic switching along the [hkl] crystallographic axis, given by $A_{hkl} = \int_{M_r}^{M_s} H \, dM$. Hysteresis loops for the entire heterostructure series are presented in Fig. S9 [30]. Our previous reported magnetic characterization of J14 films indicates no changes to magnetic ordering beyond frustration of antiferromagnetism that accompanies changes to the Co valence; further details on magnetic characterization are discussed in Refs. [5,6].

[1] C. M. Rost, E. Sachet, T. Borman, A. Moballegh, E. C. Dickey, D. Hou, J. L. Jones, S. Curtarolo, and J.-P. Maria, Nat. Commun. **6**, 8485 (2015).

[2] C. M. Rost, Z. Rak, D. W. Brenner, and J.-P. Maria, J. Am. Ceram. Soc. **100**, 2732 (2017).

[3] Z. Rák, J.-P. Maria, and D. W. Brenner, Mater. Lett. **217**, 300 (2018).

[4] D. Berardan, A. K. Meena, S. Franger, C. Herrero, and N. Dragoe, J. Alloys Compd. **704**, 693 (2017).

[5] P. B. Meisenheimer, T. J. Kratofil, and J. T. Heron, Sci. Rep. **7**, 13344 (2017).

[6] P. B. Meisenheimer, L. D. Williams, S. H. Sung, J. Gim, P. Shafer, G. N. Kotsonis, J.-P. Maria, M. Trassin, R. Hovden, E. Kioupakis, and J. T. Heron, Phys. Rev. Mater. **3**, 104420 (2019).

[7] D. Bérardan, S. Franger, A. K. Meena, and N. Dragoe, J. Mater. Chem. A **4**, 9536 (2016).

[8] D. Berardan, S. Franger, D. Dragoe, A. K. Meena, and N. Dragoe, Phys. Status Solidi - Rapid Res. Lett. **10**, 328 (2016).

[9] M. P. Jimenez-Segura, T. Takayama, D. Bérardan, A. Hoser, M. Reehuis, H. Takagi, and N. Dragoe, Appl. Phys. Lett. **114**, 122401 (2019).

[10] N. J. Usharani, R. Shringi, H. Sanghavi, S. Subramanian, and S. S. Bhattacharya, Dalton Trans. **49**, 7123 (2020).

[11] N. Osenciat, D. Berardan, D. Dragoe, B. Leridon, S. Hole, A. K. Meena, S. Franger, and N. Dragoe, J. Am. Ceram. Soc. **102**, 6156 (2019).

[12] Z. Rak, C. M. Rost, M. Lim, P. Sarker, C. Toher, S. Curtarolo, J. P. Maria, and D. W. Brenner, J. Appl. Phys. **120**, 095105 (2016).

[13] J. L. Braun, C. M. Rost, M. Lim, A. Giri, D. H. Olson, G. N. Kotsonis, G. Stan, D. W. Brenner, J.-P. Maria, and P. E. Hopkins, Adv. Mater. **30**, 1805004 (2018).

[14] J. Gild, M. Samiee, J. L. Braun, T. Harrington, H. Vega, P. E. Hopkins, K. Vecchio, and J. Luo, J. Eur. Ceram. Soc. **38**, 3578 (2018).

[15] Y. Sharma, B. L. Musico, X. Gao, C. Hua, A. F. May, A. Herklotz, A. Rastogi, D. Mandrus, J. Yan, H. N. Lee, M. F. Chisholm, V. Keppens, and T. Z. Ward, Phys. Rev. Mater. **2**, 60404 (2018).

[16] A. Sarkar, L. Velasco, D. Wang, Q. Wang, G. Talasila, L. de Biasi, C. Kubel, T. Brezesinski, S. S. Bhattacharya, H. Hahn, and B. Breitung, Nat. Commun. **9**, 3400 (2018).

[17] A. Sarkar, Q. Wang, A. Schiele, M. R. Chellali, S. S. Bhattacharya, D. Wang, T. Brezesinski, H. Hahn, L. Velasco, and B. Breitung, Adv. Mater. 1806236 (2019).

[18] N. Qiu, H. Chen, Z. Yang, S. Sun, Y. Wang, and Y. Cui, J. Alloys Compd. **777**, 767 (2019).

[19] A. Sarkar, C. Loho, L. Velasco, T. Thomas, S. S. Bhattacharya, H. Hahn, and R. Djenadic, Dalton Trans. **46**, 12167 (2017).

[20] A. Sarkar, B. Eggert, L. Velasco, X. Mu, J. Lill, K. Ollefs, S. S. Bhattacharya, H. Wende, R. Kruk, R. A. Brand, and H. Hahn, APL Mater. **8**, 051111 (2020).

[21] P. B. Meisenheimer and J. T. Heron, MRS Adv. (2020), doi:10.1557/adv.2020.295.

[22] J. Zhang, J. Yan, S. Calder, Q. Zheng, M. A. McGuire, D. L. Abernathy, Y. Ren, S. H. Lapidus, K. Page, H. Zheng, J. W. Freeland, J. D. Budai, and R. P. Hermann, Chem. Mater. **31**, 3705 (2019).

[23] Z. Rak and D. W. Brenner, J. Appl. Phys. **127**, 185108 (2020).

[24] M. R. Chellali, A. Sarkar, S. H. Nandam, S. S. Bhattacharya, B. Breitung, H. Hahn, and L. Velasco, Scr. Mater. **166**, 58 (2019).

[25] A. D. Dupuy, X. Wang, and J. M. Schoenung, Mater. Res. Lett. **7**, 60 (2019).

[26] W. Hong, F. Chen, Q. Shen, Y.-H. Han, W. G. Fahrenholtz, and L. Zhang, J. Am. Ceram. Soc. **102**, 2228 (2019).

[27] D. R. Diercks, G. Brennecka, B. P. Gorman, C. M. Rost, and J.-P. Maria, Microsc. Microanal. **23(S1)**, 1640 (2017).

[28] C. M. Rost, Ph.D. Dissertation, North Carolina State University, 2016.

[29] G. N. Kotsonis, C. M. Rost, D. T. Harris, and J.-P. Maria, MRS Commun. **8**, 1371 (2018).

[30] See Supplemental Material at http://link.aps.org/supplemental/10.1103/PhysRevMaterials.4.100401 for XRD, EDS, and AFM data showing film quality; EELS spectra; XAS spectra; film photographs and optical transmission data; all heterostructure magnetization loops; XRD of films grown on [00.1]-alumina; data fitting tables; and additional ellipsometry model representations.

[31] M. Björck and G. Andersson, J. Appl. Crystallogr. **40**, 1174 (2007).

[32] M. Y. Soomro, I. Hussain, N. Bano, E. Broitman, O. Nur, and M. Willander, Nanoscale Res. Lett. **7**, 146 (2012).

[33] R. W. G. Wyckoff, *Crystal Structures*, 2nd ed. (Interscience, New York, 1963).

[34] H. Cao, Z. Zhou, J. Yu, and X. Zhou, J. Comput. Electron. **17**, 21 (2018).

[35] C.-S. Zha, H. Mao, and R. J. Hemley, Proc. Natl. Acad. Sci. USA **97**, 13494 (2000).

[36] M. S. Selim, J. Cryst. Growth **265**, 115 (2004).

[37] C. Giovanardi, A. di Bona, S. Altieri, P. Luches, M. Liberati, F. Rossi, and S. Valeri, Thin Solid Films **428**, 195 (2003).

[38] N. G. Schmahl and G. F. Eikerling, Z. Phys. Chem. **62**, 268 (1968).

[39] J. K. Lumpp, N. Chen, K. C. Goretta, and H. M. Herro, High Temp. Mater. Process. **9**, 1 (1990).

[40] C. H. Bates, W. B. White, and R. Rustum, Science **137**, 993 (1962).

[41] R. Groenen, J. Smit, K. Orsel, A. Vailionis, B. Bastiaens, M. Huijben, K. Boller, G. Rijnders, and G. Koster, APL Mater. **3**, 070701 (2015).

[42] S. Wicklein, A. Sambri, S. Amoruso, X. Wang, R. Bruzzese, A. Koehl, and R. Dittmann, Appl. Phys. Lett. **101**, 131601 (2012).

[43] A. N. Khodan, S. Guyard, J.-P. Contour, D.-G. Crété, E. Jacquet, and K. Bouzehouane, Thin Solid Films **515**, 6422 (2007).

[44] R. F. Egerton, *Electron Energy-Loss Spectroscopy in the Electron Microscope* (Springer Science & Business Media, Berlin, 2011).

[45] Z. L. Wang, J. S. Yin, and Y. D. Jiang, Micron **31**, 571 (2000).

[46] C. F. Chang, Z. Hu, H. Wu, T. Burnus, N. Hollmann, M. Benomar, T. Lorenz, A. Tanaka, H.-J. Lin, H. H. Hsieh, C. T. Chen, and L. H. Tjeng, Phys. Rev. Lett. **102**, 116401 (2009).

[47] R. D. Shannon, Acta Crystallogr. **A32**, 751 (1976).

[48] M. Chen, B. Hallstedt, and L. J. Gauckler, J. Phase Equilibria **24**, 212 (2003).

[49] S. C. Petitto, E. M. Marsh, G. A. Carson, and M. A. Langell, J. Mol. Catal. A Chem. **281**, 49 (2008).

[50] A. Matsuda, R. Yamauchi, D. Shiojiri, G. Tan, S. Kaneko, and M. Yoshimoto, Appl. Surf. Sci. **349**, 78 (2015).

[51] D. Feeler and R. S. Williams, Mater. Res. Soc. Symp. Proc. **341**, 29 (1994).

[52] A. Kashir, H.-W. Jeong, G.-H. Lee, P. Mikheenko, and Y. H. Jeong, Thin Solid Films **692**, 137606 (2019).

[53] F. Urbach, Phys. Rev. **92**, 1324 (1953).

[54] U. Nowak, K. D. Usadel, J. Keller, P. Miltenyi, B. Beschoten, and G. Guntherodt, Phys. Rev. B **66**, 014430 (2002).

[55] C. Binek, A. Hochstrat, and W. Kleemann, J. Magn. Magn. Mater. **234**, 353 (2001).

[56] F. Radu and H. Zabel, in *Magnetic Heterostructures*, edited byH. Zabel and S. D. Bader (Springer, Berlin, 2008).

[57] F. Radu, A. Westphalen, K. Theis-Brohl, and H. Zabel, J. Phys. Condens. Matter **18**, L29 (2005).

[58] L. D. Madsen, R. Charavel, J. Birch, and E. B. Svedberg, J. Cryst. Growth **209**, 91 (2000).

[59] J. M. LeBeau, R. Engel-Herbert, B. Jalan, J. Cagnon, P. Moetakef, S. Stemmer, and G. B. Stephenson, Appl. Phys. Lett. **95**, 142905 (2009).

[60] C. Ophus, J. Ciston, and C. T. Nelson, Ultramicroscopy **162**, 1 (2016).

[61] H. G. Tompkins and E. A. Irene (Eds.), *Handbook of Ellipsometry* (William Andrew Publishing, Norwich, NY, 2005).

[62] G. E. Jellison, Thin Solid Films **234**, 416 (1993).